Applied Energy 380 (2025) 125011

Contents lists available at ScienceDirect

Applied Energy

journal homepage: www.elsevier.com/locate/apenergy

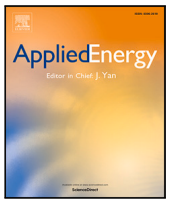

Multi-fidelity surrogate modeling of nonlinear dynamic responses in wave energy farms

Charitini Stavropoulou [a,*], Eirini Katsidoniotaki [b], Nicolás Faedo [c], Malin Göteman [a,d]

[a] Department of Electrical Engineering, Uppsala University, Sweden
[b] Department of Mechanical Engineering, Massachusetts Institute of Technology (MIT), USA
[c] Department of Mechanical and Aerospace Engineering, Politecnico di Torino, Italy
[d] Centre of Natural Hazards and Disaster Science (CNDS), Uppsala, Sweden

ARTICLE INFO

Keywords:
Multi-fidelity surrogate model
LSTM neural network
Wave energy farm
Point-absorber
Nonlinear dynamic responses
Real-time monitoring

ABSTRACT

In wave energy farms, accurately determining the motion of each wave energy converter is essential for performance evaluation, estimating energy production, and implementing effective control strategies. The primary challenge lies in the real sea environment, where the complex nonlinear hydrodynamic phenomena make it difficult to estimate the motion of each converter precisely. High-fidelity numerical simulations, such as computational fluid dynamics, offer a detailed representation of the wave farm's response to incoming waves. However, they are computationally intensive, making them impractical for real-time implementation and scenario evaluation. Conversely, although widely used in the industry, low-fidelity models based on linear potential flow theory lack accuracy and provide only a general solution trend. Experimental wave tank tests, while offering realistic, high-fidelity system representations, face limitations due to flexibility and costs. A multi-fidelity surrogate modeling approach presents a viable solution for designing and controlling wave energy farms. By leveraging data from various fidelities, low-fidelity numerical simulations, and high-fidelity experimental measurements, we develop a model capable of predicting the actual heave motion of each converter within a farm under diverse irregular wave conditions. This model effectively corrects the low-fidelity motion to align with each converter's real heave response. Central to our model is the long-short-term memory machine learning method, which enables the prediction of the devices' temporal response to incoming irregular waves. This model delivers solutions with low computational cost, making it suitable for estimating the actual device response during the design stage of a wave energy farm, facilitating real-time monitoring.

1. Introduction

The increasing worldwide energy demands and the immediate need to decrease greenhouse gas emissions drive the attention towards further exploitation of renewable energy resources [1]. Even though up to 71% of the earth's surface is covered by water, energy coming from the ocean waves is the single largest and least tapped renewable energy source on the planet [2]. With the theoretical wave energy potential being approximately 32,000 TWh/year [3–5], a possible co-location with other renewable resources [6,7], and limited environmental harm [8,9], wave energy is seen as a viable solution for a green future. Despite decades of scientific research, harvesting wave energy is still at an early stage of development, as many projects result in a higher levelised cost of energy (LCoE) compared to other renewable energy generating technologies. One way to achieve lower LCoE is to arrange multiple wave energy converters (WECs) in various array configurations, forming wave energy farms [10]. This is particularly true for point-absorbers, the largest category of wave energy concepts [11,12]. Wave farms are essential for large-scale, economically viable projects to decrease the installation, operation, and maintenance costs (per device), to enable power absorption of more than a few MW and an even power distribution [13].

However, tracking and predicting the performance of several WECs is still a challenging task due to the harsh sea environment and the complex nonlinear phenomena that arise during the interaction of the farm with the ocean waves. The WECs experience intense hydrodynamic interactions when operating in farm configurations due to the scattered and radiated waves on the free surface, which can heavily affect their overall performance. A way to model WEC dynamics with high precision is computational fluid dynamics (CFD) simulations [14–16]. For instance, in [17], a CFD model is developed for two WECs

* Corresponding author.
E-mail address: charitini.stavropoulou@angstrom.uu.se (C. Stavropoulou).

https://doi.org/10.1016/j.apenergy.2024.125011
Received 17 July 2024; Received in revised form 4 November 2024; Accepted 23 November 2024
Available online 4 December 2024

placed closely to study the heaving motion under intense hydrodynamic interactions. However, the extreme computational costs and the extensive time required, which can take several hours or days on high-performance computing systems to simulate just a few seconds of real wave farm interaction with the waves [18], make CFD an unsuitable choice for extensive wave farm studies. Simplifications are hence introduced to accomplish efficient numerical models. Under the assumption of linear potential flow theory, the fluid is presumed to be non-viscous, irrotational, and incompressible, the waves are non-steep, and the boundary conditions are linearized. Then, the fluid–structure interaction problem can be solved under a linear hydrodynamic formulation, also for large farms [19]. However, the fast linear models come at the cost of low accuracy, especially in the steepest wave environments, where the non-realistic approximations of the fluid flow result in crude estimations. One way to model wave farm dynamics accurately is through wave tank experiments. However, experimental campaigns face a lot of time constraints, utilizing only a limited amount of operating wave conditions and device set-ups due to financial limitations and fully booked wave tanks. Also, we should note that wave tank tests do not demonstrate a perfect reality either, as the sources of uncertainty include wave reflections against the tank walls, miscalculations in the friction estimation, and general imperfections in the testing equipment [20]. Even though a lot of work is integrated into wave tank campaigns worldwide, the complex nature and the high financial costs associated with such investigations make wave farm tank data scarce in wave energy. An early experimental work by [21] studies a range of WEC array effects indicating the overall power absorption and the influence on the wave climate at the deployment site. The experimental set-up incorporates arrays of up to twenty-five devices in several layouts and wave conditions. Recently, an open-access dataset of WEC farms, under the name SWELL (Standardized Wave Energy converter array Learning Library), is generated, incorporating up to five WECs and different layouts for specific wave environments, see [22].

Precise modeling of the dynamics within wave energy farms is essential for the evolution of ocean wave energy towards a commercialized and cost-effective future. Wave farms could potentially incorporate a small number to around hundreds of WECs arranged in carefully designed layouts [23,24]. Within this framework, knowing the actual responses of all the interacting devices due to a variety of wave climates could provide essential information on the necessary ocean space required, as well as the optimal farm layout, while estimating realistic economic scenarios [25,26]. Furthermore, estimating the behavior of the adjacent WECs could help investigate the environmental impact near the deployment site, especially assessing the change of the wave climate, so the wave height and wave power, by tracking the perturbed wave field around the farm [27,28]. Also, insightful modeling of WEC dynamics is tied to developing efficient control strategies for maximizing power absorption in response to certain wave environments while monitoring the converters' physical constraints [29–32]. Essentially, having access to an accurate farm tool, one can predict actual power absorption limits while estimating any risks for a safe grid integration [33–35]. Therefore, the reliability of the utilized model is a key issue. Practically, wave farm models need to represent response scenarios as close to reality as possible to aid the various phases of progress within a wave energy farm concept. This challenge leads to the ultimate question on *'how to develop an accurate and efficient tool to simulate several interacting WECs in various wave environments?'* To address this question, we introduce a multi-fidelity machine learning model based on long-short-term memory (LSTM) neural networks for the prediction of WEC motion within wave energy farms.

Recently, machine learning models for predicting the temporal dynamics of marine structures have gained significant attention. To be exact, several data-driven approaches incorporating LSTM networks for time-series forecasting are generating a growing interest in marine technology systems. For instance, in [36], the dynamic mooring line tension is predicted using a floating platform's motion response data, while in [37], the mooring line response of a vessel is monitored with high precision, using its motion as the input signal. Another case can be found in [38], where a mooring line failure of a floating structure is detected in almost real-time, based on simulated motion data generated using actual environmental conditions. In the framework of wave energy converter concepts, in [39], an LSTM network is used to correct the time series of mooring line force data of a point-absorber WEC, focusing on the extreme peaks. Also, in [40], an LSTM network is developed to accurately forecast the power output of a wave energy converter named "Searaser". While in [41], a hybrid deep-learning model incorporating LSTM networks is developed to predict wave heights in near real-time to assist the accurate estimation of energy generation. Moreover, LSTM networks are widely used in ship responses evaluation: for example, in [42], a real-time ship motion forecaster is developed to provide fast predictions with levels of accuracy that can approximate those of high-fidelity tools while, in [43], an LSTM network is used to learn the nonlinear wave propagation and the roll motion of a ship section in beam seas. Another case can be found in [44] where the main vessel motions, *e.g.*, pitch, heave, and roll, are forecasted using as input stochastic characterization of the wave elevation for a particular sea state.

Within the context of data-driven methods, we focus on the so-called multi-fidelity class of surrogate models, [45–47]. Such methods incorporate an information fusion when data from various fidelities are accessible, [48,49]. Usually, two complexity levels are incorporated and labeled as low-fidelity and high-fidelity data. However, there is no restriction on the number of utilized fidelities. In general, high-fidelity data represent very accurate measurements; however, they have been obtained using high computational models or have intense financial costs. On the other hand, low-fidelity data have a reduced accuracy and are less expensive to obtain. Therefore, multi-fidelity approaches integrate several sources of diverse fidelities into a single model. In real-world applications, merely a limited amount of high-fidelity data is accessible, while lower-fidelity data could be in great quantity. So, one of the main motives for incorporating multi-fidelity techniques is to enhance a dataset of sparse and expensive measurements using a wide range of inexpensive lower-fidelity data. A comprehensive framework of multi-fidelity modeling to function approximation and inverse PDE problems is presented in [50], where linear and nonlinear correlations between the low- and high-fidelity data are investigated. Also, in [51], an extensive multi-fidelity approach is studied, incorporating a validation set using wind turbine simulations. Further in [52], Bayesian and physics-informed neural networks are integrated into a multi-fidelity approach to capture the cross-correlation with uncertainty quantification between the low- and high-fidelity data. We note that the specific surrogate technique integrated within the multi-fidelity approach is part of the design procedure. For example, in [53], a multi-fidelity technique is developed based on the nonlinear autoregressive Gaussian process method and graph convolutional networks for predicting the deformation of fish net cages within aquaculture farms. Similar to the approach adopted in our work, in [54], a multi-fidelity surrogate model based on an LSTM neural network is investigated by combining low-fidelity and high-fidelity ship motion responses in waves; the proposed method improves the fidelity of the reduced-order model relative to the higher-order component while retaining high computational efficiency.

Despite the great potential of multi-fidelity techniques in handling effectively sparse high-fidelity datasets, such methods are not quite integrated within wave energy concepts. Noting the experimental limitations in wave energy generating technologies and the necessity of valid models for performance estimation in wave energy farms, we present a method based on an LSTM network utilizing a multi-fidelity dataset for the accurate heave motion prediction of multiple interacting point-absorber WECs. Point-absorbers are heaving devices moving mainly in the vertical direction as well as in surge in response to the incident waves. Estimating accurately the vertical motion of the floats is challenging due to the intense hydrodynamic interactions on the free

surface. However, the quest for accurate or optimized heave motion is not new to the wave sector. In [55], the hydrodynamic shape of a floating buoy is optimized for maximizing the heave motion response. While in [56], nonlinear effects that influence the dynamics of the heave motion for a point-absorber are investigated. Frequently, the heaving mode is characterized as the dominant degree of freedom, as in many operational conditions, the device's movement in other directions is not as significant. So, the precise modeling of the heaving motion allows for a better design and tuning of the power take-off (PTO) system, ensuring that the system resonates with the incoming waves. Due to the main characteristics of generator technologies, even if the floats move in several directions, most of the PTO motion is triggered by heave; other degrees of freedom, like surge, usually excite the PTO in a smaller proportion. Constraining a point-absorber to heave motion can be a good approximation for a six degree of freedom moored device. In [57], it is shown that a heave-only point-absorber WEC does well at estimating the power capture for a six degree of freedom moored device. The six degree of freedom configuration had only a slight shift in the resonant period. Therefore, the heave mode is a good indicator of energy conversion.

The suggested model incorporates two fidelity levels. The low-fidelity data corresponds to the heave motion of three interacting point-absorber WECs placed in a row. The low-fidelity heave is obtained by an in-house linear potential flow scheme. The corresponding high-fidelity data are extracted from an experimental dataset. The experimental set-up corresponds to a 1:10 scaled prototype of an array of point-absorber WECs. The proposed LSTM network practically maps the incoming wave field and the corresponding simplified heave responses of three interacting WECs to the sophisticated, real-time heave motion of the devices coming from an experimental wave tank test. We highlight that the experimental heave data results from the multi-degree-of-freedom motion of the point-absorbers, and their interacting behavior. The primary goal of the multi-fidelity method is to correct the low-fidelity WEC responses using knowledge of the high-fidelity experimental data. The proposed LSTM is chosen after a thorough sensitivity analysis, while the so-called hyperparameters of the network are selected via the control variable method. Furthermore, the corrected WEC responses are compared with linear data-based modeling techniques, showing a significant improvement in terms of accuracy when evaluated against the experimental data. Finally, to fully exploit the multi-fidelity method, using the black-box mapping between the simplified motion and the *actual* experimental motion, we reconstruct the full nonlinear responses in unseen wave environments so that they closely match the experimental measurements using as input the incoming wave and the low-fidelity linear potential flow data.

We show that by supplying the simplified motion of multiple interacting WECs using low-fidelity simulation data, the model can recreate the experimental motion of the devices for new wave environments while retaining a small computational cost. To emphasize the value of the proposed methodology, using a few targeted waves and the corresponding linear potential flow responses during training, we show that the LSTM model can forecast the *actual* motion of the WECs for unseen waves, *i.e., operating conditions which were not supplied during the training phase*. We highlight that while the experiments can capture the fully nonlinear behavior of several interacting WECs, only a very limited set of conditions is tested due to time restrictions and operational costs. On the other hand, the multi-fidelity method can create fully nonlinear dynamics of several interacting WECs while retaining a minimum cost. This approach can be beneficial for fine-tuning experimental campaigns by arranging several related operational conditions and ultimately filling a substantial knowledge void in modeling realistically and efficiently the simultaneous motion of multiple interacting WECs.

The remainder of the paper is organized as follows. Section 2 gives a detailed account of the physical experiment and the linear potential flow model, so the high- and low-fidelity data. It also features the theoretical framework, presenting the system identification method and the fundamental aspects of the LSTM network. Section 3 presents a detailed account of the obtained results and corresponding discussion, while Section 4 encompasses the main conclusions from our study.

Table 1
Experimental radius and draft, the generator damping is γ and water depth in the wave tank is $\bar{h}$.

Buoy radius	R_{exp} = 0.244 [m]
Buoy draft	d_{exp} = 0.0948 [m]
Damping	γ = 306 [Ns/m]
Water depth	$\bar{h}$ = 2.5 [m]

Table 2
Characteristics of the incoming waves. The significant wave height H_s, the peak period T_p, the wave duration T_{wave}, and the corresponding steepness.

WaveID	H_s [m]	T_p [s]	T_{wave} [min]	Steepness [-]
IW1	0.1482	1.2488	6.83	0.0609
IW2	0.1561	1.6787	6.83	0.0355
IW3	0.1598	1.8893	6.83	0.0287
IW4	0.1609	2.5473	6.83	0.0159
IW5	0.1615	3.1411	6.83	0.0105

2. Methods

2.1. Experimental method

The high-fidelity data used within this study is taken from an experimental wave tank dataset. The experimental campaign was conducted at the COAST Lab at the University of Plymouth, UK. The data corresponds to a layout configuration including six WECs placed in a symmetric grid, with one pair in each row. The set-up represents a 1:10 scaled prototype of an array of point-absorbers, based on the WEC concept developed at Uppsala University [11]. The physical layout comprises six elliptical buoys, moving in six degrees of freedom. To measure the motion, each buoy is equipped with five reflective markers. The markers are tracked by a set of eight Qualisys cameras. Each buoy is connected to a PTO system. The PTO is performed by passive damping using a system exclusively designed for the wave tank experiment. A damping value of γ = 306 Ns/m is used for all the converters; see [58,59]. The array set-up is shown in Fig. 1, while the WEC and system specifications are presented in Table 1. Due to the symmetric properties of the considered layout, we focus on WECs A, C, and B, *i.e.*, on a single row of devices. The responses of the WECs are studied in five wave environments, all generated within the basin. In particular, the sea states considered are represented by five irregular waves (IWs) obtained from a Bretschneider spectrum. Note that, in [58], data acquisition of the free-surface elevation is performed simultaneously with motion acquisition, i.e., in the same experimental test. This is done to avoid incorporating, within the data-based modeling procedure, the uncertainty that arises when attempting to generate the same wave realization more than once within the mechanical wavemaker system. The irregular waves align with conditions near the natural period of the WECs. The water density is ρ = 1000 kg/m^3, and the sampling frequency for data acquisition is 128 Hz, with a corresponding sampling time of 0.0078 s, while every wave lasts 6 min and 50 s. Each incoming wave is defined by its steepness, which is determined by $s = (2\pi H_s)/(gT_p^2)$, where H_s is the significant wave height, g = 9.81 m/s^2 is the acceleration due to gravity and T_p is the peak period. A detailed account of the waves considered is given within Table 2.

2.2. Linear potential flow model

The low-fidelity data used in this work is obtained from a linear potential flow numerical scheme. Assuming that the forces acting on a system of interacting floating bodies are either functions of the system's state or the wave properties, we can apply a standard linear time-domain modeling framework based on Cummins' formulation [60]. The equations of motion for an array of interacting WECs subject to wave and other external forces boil down to solving a system of

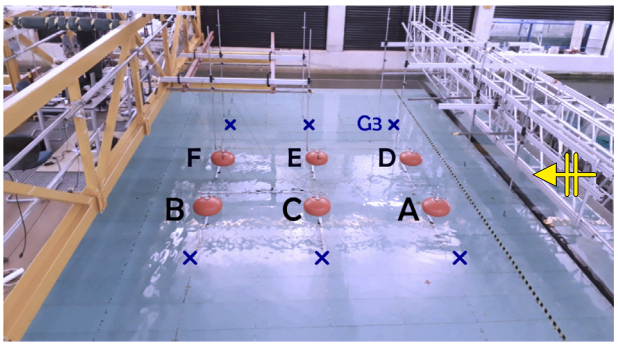

Fig. 1. Experimental set-up. The arrow on the right indicates the wave direction, and G3 denotes the gauge that measures the wave elevation.

Volterra integro-differential equations of the convolution type [61], particularly involving impulse response functions to describe excitation and radiation effects. In the simplified numerical model, the buoys are assumed to move in *heave only*. It should be emphasized that the buoys in the experiments are moving freely in six degrees of freedom. Thus, the numerical model simplifies two critical characteristics of the actual system: the fluid flow by assuming linear potential flow theory and the buoy dynamics by assuming only heave motion. Also, in the numerical scheme, the connection mooring line between the buoy and the PTO system is considered non-slack. Therefore, nonlinear dynamics arising from slack-line conditions is neglected, see [62]. Within the discussed conditions, the equations of motion for the WECs can be described by the following system of equations,

$$(M + M^{add}(\infty))\ddot{\boldsymbol{z}}(t) = \boldsymbol{f}_e(t) - \int_0^t K(t-\tau)\dot{\boldsymbol{z}}(\tau)\mathrm{d}\tau + \boldsymbol{f}_h(t) + \boldsymbol{f}_{PTO}(t) - \boldsymbol{w}, \tag{1}$$

where $M \in \mathbb{R}^{n\times n}$ is a diagonal matrix containing the mass of each WEC m_j, with $j \in \{1,\dots,n\}$, while $M^{add}(\infty) \in \mathbb{R}^{n\times n}$ is the matrix containing the so-called added mass at the infinity frequency limit, for each pair i-j of interacting point-absorbers, where $\{i,j\} \subset \{1,\dots,n\}$. The vector $\boldsymbol{z}(t) = (z_1(t),\dots,z_n(t))^T$ contains the vertical displacement of each device, while the excitation force is defined as $\boldsymbol{f}_e(t) = (f_{e_1}(t),\dots,f_{e_n}(t))^T$. Note that $\boldsymbol{f}_e(t)$ depends on the free-surface elevation, which, for a suitable fixed point in space, is denoted as $e(t) \in \mathbb{R}$. The convolution operation in (1) represents the radiation term, where $K(t) \in \mathbb{R}^{n\times n}$, $K_{ij} \in L^2(\mathbb{R})$, is the radiation impulse response function. Similarly, $\boldsymbol{f}_h(t)$ is the hydrostatic buoyancy force, $\boldsymbol{f}_{PTO}$ is the applied force from the PTO system, and $\boldsymbol{w} = (m_1 g,\dots,m_n g)^T$ is the vector containing the weights. The hydrodynamic coefficients of the excitation and radiation force for the elliptical buoys are computed using the boundary element method software WAMIT. As the draft of ellipsoids is defined to be half of the buoy height in WAMIT, the radius of the buoys in the numerical model is $R_{num} = 0.2173$ m, which is slightly smaller than in the experimental set-up. This ensures that the experimental and numerical buoys have the same submerged volume. A detailed explanation of the numerical solution of Eq. (1) can be found in [63].

2.3. Multi-fidelity surrogate model workflow

Fig. 2 demonstrates the workflow of the multi-fidelity surrogate model, incorporating the data described in Sections 2.1 and 2.2. The proposed method is designed to predict the motion within a wave energy farm, while it can be extended to any farm layout or number of WECs. Initially, within the wave tank, wave gauge number 3 (G3), see Fig. 1, measures the elevation of the incoming wave field. The five measured irregular waves used in the basin, see Table 2 serve as input to the low-fidelity, linear potential flow scheme described in Section 2.2. The simplified model is implemented in MATLAB and estimates the responses of three interacting devices arranged in a row. We note that the modeled responses correspond to the time series of the heave motion. Then, the incoming irregular waves and the low-fidelity time series of WECs A, C, and B (see Fig. 1) serve as input to the LSTM model. The network learns the mapping between the low-fidelity input and high-fidelity output, *i.e., the targeted experimental heave*. In other words, the network learns how to refine the low-fidelity responses based on a sophisticated high-fidelity output of the real-time heave motion of the devices within the wave tank. After sufficient training, the network yields heave predictions that closely match the real WEC responses measured in the wave basin. The proposed LSTM model integrated within the multi-fidelity approach can be seen as a parallel multi-input, multi-output network, correcting the simultaneous motion of three interacting devices in five sea states.

2.4. System identification method

An alternative linear representation to that derived via physical principles in Eq. (1) can be achieved by leveraging tools from the field of system identification. In particular, using measurements of the free-surface elevation $e(t)$, according to the available wave gauges described in Fig. 1, and the corresponding motion of the interacting WECs $\boldsymbol{z}(t)$, an input–output dynamical linear map can be inferred via standard frequency-domain identification techniques, as detailed in [64]. Though beyond the scope of this paper, which is focused on developing and applying more complex machine learning models in the WEC field, a brief account of the considered standard linear system identification techniques is provided in the following to keep the current work reasonably self-contained.

Standard frequency-domain system identification is virtually always decomposed into a two-stage process, in which a non-parametric system response is first estimated [65], leveraging the Fourier transform of each corresponding input–output pair. This empirical non-parametric response is then approximated in terms of a parametric structure, *i.e.* a transfer function $G \in \mathcal{H}_\infty$, $G(\mathrm{s}) \in \mathbb{C}^{n\times 1}$, with s the Laplace variable and $\mathcal{H}_\infty$ the Hardy space of all complex-valued functions which are analytic and of bounded modulus in the open right half-plane, mapping the free-surface elevation with each corresponding WEC device output, that is:

$$Z(\mathrm{s}) = G(\mathrm{s})E(\mathrm{s}), \tag{2}$$

where $\{Z(\mathrm{s}), E(\mathrm{s})\} \subset \mathbb{C}^{n\times 1} \times \mathbb{C}$ denote the Laplace transform of the WEC motion $\boldsymbol{z}(t)$ and free-surface elevation $e(t)$, respectively. A graphical appraisal of both the estimated non-parametric frequency response (transparent, cyan) and the parametric transfer function $G(\mathrm{s})$, for devices A, C, and B in the WEC array of Fig. 1, can be appreciated in the Bode plot[1] of Fig. 3. The empirical estimates have been computed using all five sea-states described in Table 2 and their respective output signals (motions) for each WEC in the tested layout.

2.5. Long-short-term memory neural networks

LSTM neural networks are a variation of recurrent neural networks (RNNs) capable of learning dependencies in sequence prediction problems [66]. This behavior is indeed desired, especially in complex domains requiring time series forecasting. The key aspect of LSTM is its complex cell unit, incorporating gated activation functions, see Fig. 4. This design controls the ability of the network to persist information while avoiding the exploding or vanishing gradient descent problem that appears in traditional RNNs. The main components of the LSTM unit are the cell state $\boldsymbol{c}_t \in \mathbb{R}^{h\times 1}$, the hidden state $\boldsymbol{h}_t \in \mathbb{R}^{h\times 1}$, where h is

[1] A Bode plot showcases the so-called frequency-response function of $G(\mathrm{s})$ when $\mathrm{s} = \jmath\omega$. The upper plot illustrates the magnitude (in decibels) of the complex number $G(\jmath\omega)$, while the bottom plot presents its phase (in degrees).

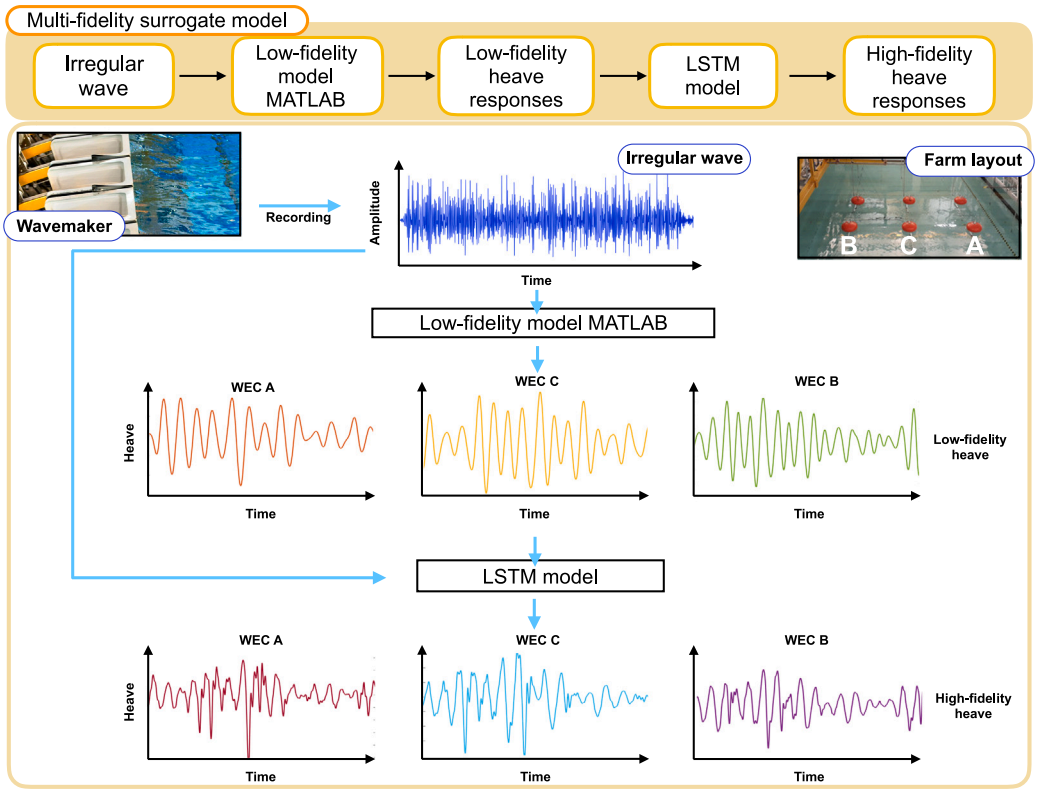

Fig. 2. Multi-fidelity surrogate model workflow. The realistic heave motion responses of three interacting WECs (A, C, and B) located in the bottom row of a symmetric array layout are modeled using low-fidelity numerical simulations and high-fidelity experimental measurements.

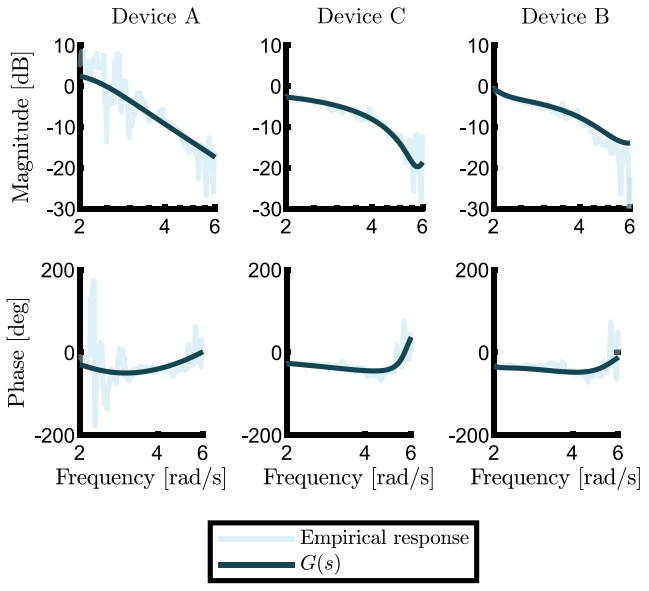

Fig. 3. Bode plot of non-parametric and parametric estimates for the linear data-based model $G(s)$ as in Eq. (2).

the so-called hidden size, see Section 2.7.1, and the gates, namely the forget, the input, and the output gate. The cell state is responsible for collecting data from all previous time steps; therefore it is the long-term memory of the network, whereas the hidden state is meant to capture the information related mostly to the previous time step, so it represents the short-term memory.

In Fig. 4, we see that, in the forget gate, the current input $\boldsymbol{x}_t \in \mathbb{R}^{d\times 1}$, and the hidden state of the previous time step $\boldsymbol{h}_{t-1}$ are combined with two sets of weights $W_{f_x} \in \mathbb{R}^{h\times d}$, $W_{f_h} \in \mathbb{R}^{h\times h}$ accordingly. The weighted sum is added to a bias term $\boldsymbol{b}_f \in \mathbb{R}^{h\times 1}$, and the result is fed into the sigmoid activation function $\sigma : \mathbb{R}^{h\times 1} \to [0,1]^h$, which turns the output into a set of values between 0 and 1, namely $\boldsymbol{f}_r \in \mathbb{R}^{h\times 1}$. Note that a value between 0 and 1 acts as a scalar operator able to amplify or nullify a certain quantity. $\boldsymbol{f}_r$ is multiplied element-wise by the previous long-term memory $\boldsymbol{c}_{t-1}$. Therefore, the forget gate determines the percentage of long-term memory meaningful to the LSTM. For instance, if the forget gate outputs a vector of values close to 1, based on the current input $\boldsymbol{x}_t$, the gate deems the time series history highly significant. Consequently, when the previous time step's cell state is multiplied by the forget gate's output, the cell state retains most of its original value, effectively 'remembering' its past. Conversely, if the forget gate outputs values close to 0, the cell state's values diminish significantly, suggesting that the network should disregard much of its history until now.

Subsequently, as per Fig. 4, the input gate determines the new long-term memory $\boldsymbol{c}_t$. On the right side, the current input and the previous hidden state are weighted by a different set of weights accordingly W_{c_x}, W_{c_h} and the outcome is added to a bias term $\boldsymbol{b}_c$, the result is fed to the tangent activation function, which returns a set of values $\boldsymbol{f}_c$, between -1 and 1. Namely, $\boldsymbol{f}_c$ is the new potential long-term memory of the LSTM. On the left side of the input gate, using the sigmoid activation function and following an analogous procedure, a set of percentage values $\boldsymbol{f}_i$ is produced, which is multiplied by $\boldsymbol{f}_c$ to decide which portion of the new potential long-term memory is added to the existing long-term memory of the network. The output gate determines the new hidden state, or short-term memory $\boldsymbol{h}_t$, to be passed on. The long-term memory, $\boldsymbol{c}_t$, serves as input to the output gate, while the tangent activation function produces $\boldsymbol{f}_{c_o}$. The current input and the previous hidden state are combined using weights and biases, and the result is fed into the sigmoid activation function, which decides what percentage $\boldsymbol{f}_o$ of the potential short-term memory $\boldsymbol{f}_{c_o}$ needs to be sent

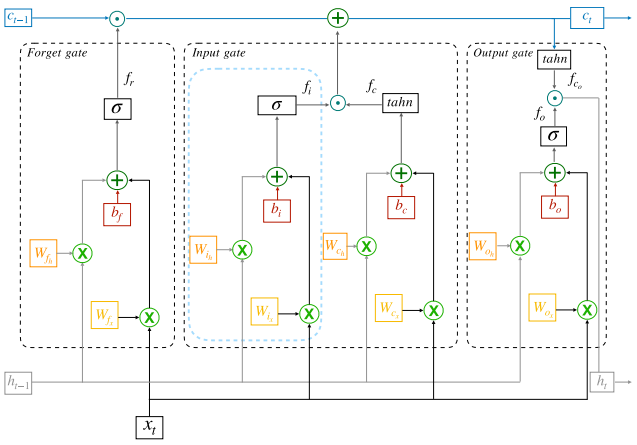

Fig. 4. LSTM unit cell.

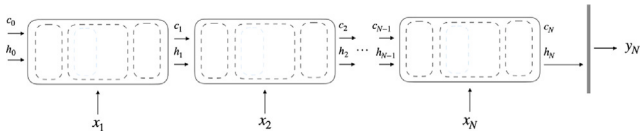

Fig. 5. LSTM and dense layer.

to the next LSTM unit. In summary, the mathematical procedure for each gate can be defined in terms of the following operations:

$$
\begin{aligned}
\boldsymbol{f}_r &= \sigma(W_{f_x}\boldsymbol{x}_t + W_{f_h}\boldsymbol{h}_{t-1} + \boldsymbol{b}_f),\\
\boldsymbol{f}_i &= \sigma(W_{i_x}\boldsymbol{x}_t + W_{i_h}\boldsymbol{h}_{t-1} + \boldsymbol{b}_i),\\
\boldsymbol{f}_c &= \tanh(W_{c_x}\boldsymbol{x}_t + W_{c_h}\boldsymbol{h}_{t-1} + \boldsymbol{b}_c),\\
\boldsymbol{c}_t &= \boldsymbol{f}_i \odot \boldsymbol{f}_c + \boldsymbol{f}_r \odot \boldsymbol{c}_{t-1},\\
\boldsymbol{f}_{c_o} &= \tanh(\boldsymbol{c}_t),\\
\boldsymbol{f}_o &= \sigma(W_{o_x}\boldsymbol{x}_t + W_{o_h}\boldsymbol{h}_{t-1} + \boldsymbol{b}_o),\\
\boldsymbol{h}_t &= \boldsymbol{f}_{c_o} \odot \boldsymbol{f}_o,
\end{aligned}
\tag{3}
$$

where the weight matrices for the input vector $\boldsymbol{x}_t$ are denoted as $\{W_{f_x}, W_{i_x}, W_{c_x}, W_{o_x}\} \subset \mathbb{R}^{h\times d}$ and the weight matrices corresponding to the hidden state $\boldsymbol{h}_t$ are denoted as $\{W_{f_h}, W_{i_h}, W_{c_h}, W_{o_h}\} \subset \mathbb{R}^{h\times h}$. The bias terms are $\{\boldsymbol{b}_f, \boldsymbol{b}_i, \boldsymbol{b}_c, \boldsymbol{b}_o\} \subset \mathbb{R}^{h\times 1}$. Finally, the operator $\odot$ denotes the standard Hadamard product, *i.e.*, element-wise multiplication. A prediction is based on multiple inputs $\{\boldsymbol{x}_1, \dots, \boldsymbol{x}_N\}$ for a certain amount of time steps $t \in \{1, \dots, N\}$. Therefore, multiple LSTM cell units are arranged, forming an LSTM layer, as per Fig. 5. The hidden state of the last cell $\boldsymbol{h}_N$ serves as input to a dense layer, which produces the output of the network $\boldsymbol{y}_N \in \mathbb{R}^{q\times 1}$, where q is the output dimension, according to the following relation:

$$
\boldsymbol{y}_N = W_d\boldsymbol{h}_N + \boldsymbol{b}_d. \tag{4}
$$

Since no activation function is applied, the dense layer is referred to as *linear*. In Eq. (4), $W_d \in \mathbb{R}^{q\times h}$ and $\boldsymbol{b}_d \in \mathbb{R}^{q\times 1}$ are the weight matrix and bias term of the dense layer.

2.6. LSTM loss function

The LSTM network is trained using the gradient descent optimization algorithm to minimize the so-called loss function. The chosen loss function measures the difference between the LSTM corrected and the experimental heave displacement values, assessing the overall error of the model's prediction. During the training period, the network weights and biases are repeatedly updated to minimize the loss over each assessment. We note that the choice of the loss function always depends on the studied problem. Here, the mean squared error is used, as it is more sensitive to outliers, to penalize any larger errors that can be encountered within the training phase. The loss function is computed as:

$$
\mathrm{MSE} = \frac{1}{s}\frac{1}{n}\sum_{i=1}^{s}\sum_{j=1}^{n}(y_j^{true} - y_j^{LSTM})_i^2. \tag{5}
$$

In particular, to train the LSTM, the dataset is usually split into several batches, each batch containing s samples, with each sample corresponding to a time step i, as per Section 2.7.2. Therefore, in Eq. (5), the error between the experimental heave y^{true} and the corresponding LSTM corrected heave y^{LSTM} is computed for each sample, and the batch-average error is calculated. Since the LSTM involves n parallel outputs, namely WECs A, C, and B, within each sample, the average error of the outputs is taken.

2.7. LSTM hyperparameter selection

The training procedure of the LSTM network can be formally defined in terms of an optimization problem, meaning that its performance heavily relies on tuning the so-called hyperparameters. Among these variables are the number of hidden layers, the hidden size, the batch size, and the window size. A proper selection is crucial to obtain a high network performance, improving the predicted values' accuracy. For this problem, one LSTM layer followed by a linear dense layer is chosen as it provides accurate results within a reasonable training time. We use the control variable method to further construct the optimal LSTM model, following the steps: the hidden size is tuned while the rest of the hyperparameters are fixed to specific initial values. Once the optimal hidden size is chosen, it is kept the same while the batch size is considered, and the window size remains at its initial value. Since the optimal hidden and batch sizes are determined, they are kept fixed while the window size is tuned. The hyperparameter selection is described to a greater extent in Sections 2.7.1–2.7.3.

The predicted time series are compared to the experimental heave displacement using the mean absolute error (MAE). The MAE offers a standard and straightforward assessment of the overall discrepancy between the predicted and the experimental responses, the latter being our ground truth model, providing a direct and intuitive norm. In particular, the MAE between the LSTM corrected and the experimental heave is measured for WECs A, C, and B in all the available sea states, see Fig. 1 and Table 2. To account for the different wave environments, the MAE is normalized with the maximum value of the corresponding experimental heave displacement of each WEC as

$$
\mathrm{NMAE} = \frac{\frac{1}{L}\sum_{i=1}^{L}|y^{true} - y^{LSTM}|_i}{\max\{|\boldsymbol{y}^{true}|\}}, \tag{6}
$$

where $L \in \mathbb{N}$ is the length of the examined time series, y_i^{true} and y_i^{LSTM} are the variables corresponding to the experimental and the LSTM corrected heave displacement for each WEC, at the time step i, whereas $\boldsymbol{y}^{true}$ denotes the fully examined time series of the experimental heave for each WEC. Based on Eq. (6), the following hyperparameters are chosen:

2.7.1. Hidden size

The hidden size can have a significant impact on prediction accuracy and is analogous to the number of neurons within each LSTM unit cell. In practice, the hidden size is the value of h discussed in Section 2.5, and it, therefore, determines the dimension of the hidden state, the cell state, and the corresponding weight matrices and bias terms along with the operations described in Section 2.5. Usually, larger hidden sizes can result in more sophisticated networks, yet increasing the required training time. However, it is well-known that if the complexity of the network surpasses a certain size, overfitting may occur. To assess the overall impact of the parameter h, we compare the prediction accuracy for four choices, namely, 16, 32, 64, and 128 hidden sizes. The results are presented in Figs. 6(a) and 7(a). The batch

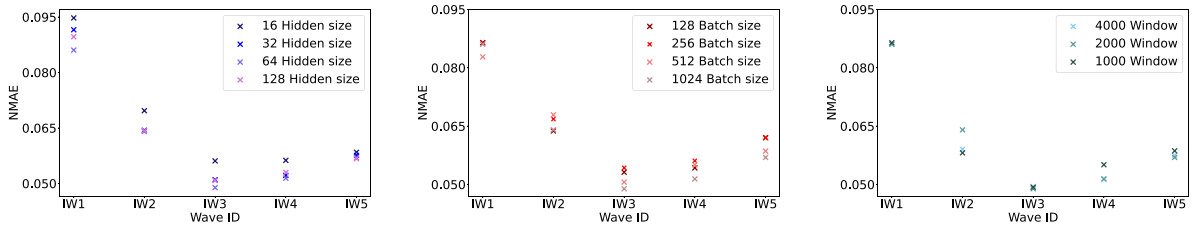

Fig. 6. Average normalized MAE (NMAE) according to Eq. (6) of the LSTM corrected heave displacement for WECs A, C, and B, located at the bottom row of the symmetric grid in Fig. 1, over all the irregular sea states in Table 2. In (a), the average NMAE is compared for 16, 32, 64, and 128 hidden size choices. In (b), the average NMAE is compared for 128, 256, 512, and 1024 batch size choices. In (c), the average NMAE is compared for time windows of 1000, 2000, and 4000 time steps.

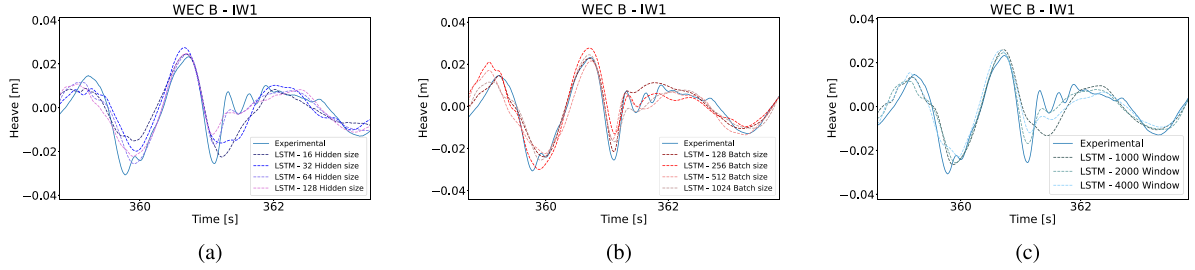

Fig. 7. Time series of the heave motion for WEC B in response to the steepest irregular wave IW1. In (a), the LSTM corrected motion is plotted for 16, 32, 64, and 128 hidden size choices. In (b), the motion is plotted for 128, 256, 512, and 1024 batch size choices. In (c), the motion is plotted for time windows of 1000, 2000, and 4000 time steps. We focus on a peak in the heave motion.

and window size must remain fixed while selecting the appropriate hidden size. Therefore, these hyperparameters are initialized to 1024 samples and 2000 time steps accordingly. The 64 hidden size is used, as the average NMAE of all the WECs is the minimum in most sea states, see Fig. 6(a), while the computational efficiency over the 128 hidden size choice is significant.

2.7.2. Batch size

The batch size is a hyperparameter of the gradient descent optimization algorithm. It defines the number of samples the model works through before updating its internal model parameters, namely the weights and the bias terms, *i.e.*, it is the value of s in Eq. (5). The training dataset can be divided into one or several batches: the smaller the batch size, the more computationally expensive the gradient descent becomes, as the frequent updates result in noisy convergence and high training times. Bigger batch sizes have more stable error gradients that could lead to early convergence, though requiring significant computer memory. We compare batch sizes of 128, 256, 512, and 1024 samples, as per the results presented in Figs. 6(b) and 7(b). The hidden size is fixed at the optimal value of 64 units, previously obtained, while the window size remains at the initial value of 2000 time steps. The 1024 batch size is chosen; although it requires the highest computer memory, it provides the minimum average NMAE in most sea states, see Fig. 6(b), within a reasonable training time.

2.7.3. Window size

The window size specifies the number of consecutive time steps the LSTM model considers to make a prediction, *i.e.*, the window size is the value N in Eq. (4). Usually, the more time steps the LSTM considers, the more internal dependencies it learns within the studied time series. We compare three different windows for 1000, 2000, and 4000 time steps, see Figs. 6(c) and 7(c). The hidden and batch sizes are kept to the optimal values of 64 units and 1024 samples previously determined. 2000 time steps are chosen as a window size as it provides the minimum average NMAE in most sea states, see Fig. 6(c) while retaining significantly shorter training time than the window size of 4000 time steps.

Table 3
LSTM hyperparameters.

Window size	2000
Batch size	1024
Hidden units	64
Features	4
learning rate	0.001
optimizer	Adam

The Adam gradient descent method [67] with an adaptive learning rate is chosen, with an initial value of 0.001. The learning rate is a small number between 0 and 1, which determines the number of steps taken during the optimization, *i.e.*, it controls how quickly the model's parameters are updated. An Early-bird stopping checkpoint is employed within the LSTM model, with a patience of 50 epochs, meaning that if there is no improvement in the validation loss for 50 consecutive epochs, the training is effectively stopped while saving the best-trained model so far. The process uses a dual Intel Xeon Gold 6130 CPU with 412 GB RAM. For time series training, longer computational times are essential, to a more significant extent, as the supported network involves a parallel multi-input and multi-output set-up. The final choice of hyperparameters in Table 3 is made to balance the prediction accuracy and the computational efficiency. Using a 70/30 data split a total of approximately 21 h is used for training. Once the network is trained, the solution is obtained within a few seconds.

3. Results & discussion

3.1. Heave motion prediction

Using the model defined in Table 3, in Figs. 8(a)–8(c) we plot the heave motion of the WECs placed in the bottom row of the symmetric grid, see Fig. 1, namely WECs A, C, and B, in response to the steepest wave environment IW1, see Table 2. The presented time series correspond to a limit within our wave range; the plotted results in this section represent the data used for testing. We focus on a peak in the motion of the devices towards the end of the time series. The numerical

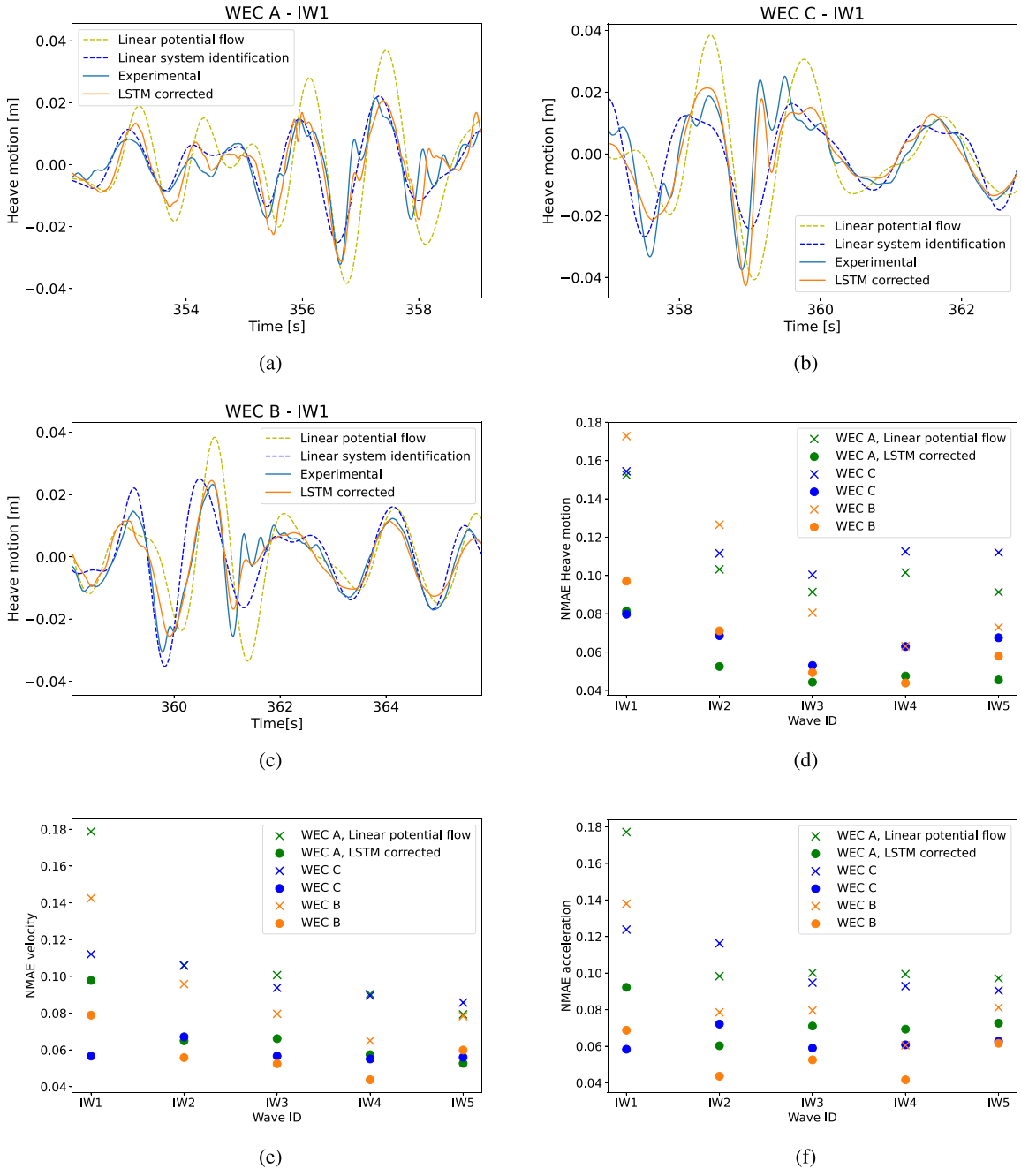

Fig. 8. In plots (a), (b), and (c), the time series of the linear potential flow, the linear system identification, the experimental and the LSTM corrected heave motion of WECs A, C, and B, located at the bottom row of the symmetric grid in Fig. 1, are presented. The time series correspond to the data used for testing. We focus on a peak towards the end of the time series. The motion of the devices is shown in response to IW1 in Table 2. In plot (d), the normalized MAE (NMAE) according to Eq. (6) for WECs A, C, and B is shown. The error corresponds to the heave motion of the devices in response to all the irregular wave environments in Table 2. The error is normalized with the maximum value of the corresponding experimental heave displacement of each WEC. In plots (e) and (f) the NMAE for the derived velocity and acceleration are shown for every WEC in response to all the available sea states.

results are obtained from the linear potential flow and the linear system identification model, see Sections 2.2 and 2.4, while the corrected heave motion is obtained from the LSTM network. The amplitude and the phase of the numerical signals are significantly improved using knowledge of the experimental data. The linear system identification model already shows a greater improvement over the linear potential flow component; however, only the LSTM corrected time series can capture the formation of the ripples within the heave motion, namely the nonlinear behavior.

We underline that the LSTM network corrects the simultaneous motion of three interacting WECs in a variety of sea states, where a single irregular wave represents each state, so the model maps a simplified input to a sophisticated output for five different waves, see Table 2. This initiates a discussion regarding the generalization properties of our model. Since a single network handles in parallel three interacting WECs in a range of five sea states, which show significant differences in wave steepness, the question arises on *how much improvement can the model provide in each sea state?* Therefore, in Fig. 8(d), we plot the normalized MAE according to Eq. (6) for every interacting WEC in response to all the irregular waves. Here, the normalized MAE is computed for both the linear potential flow heave displacement and the LSTM corrected heave displacement against the experimental motion

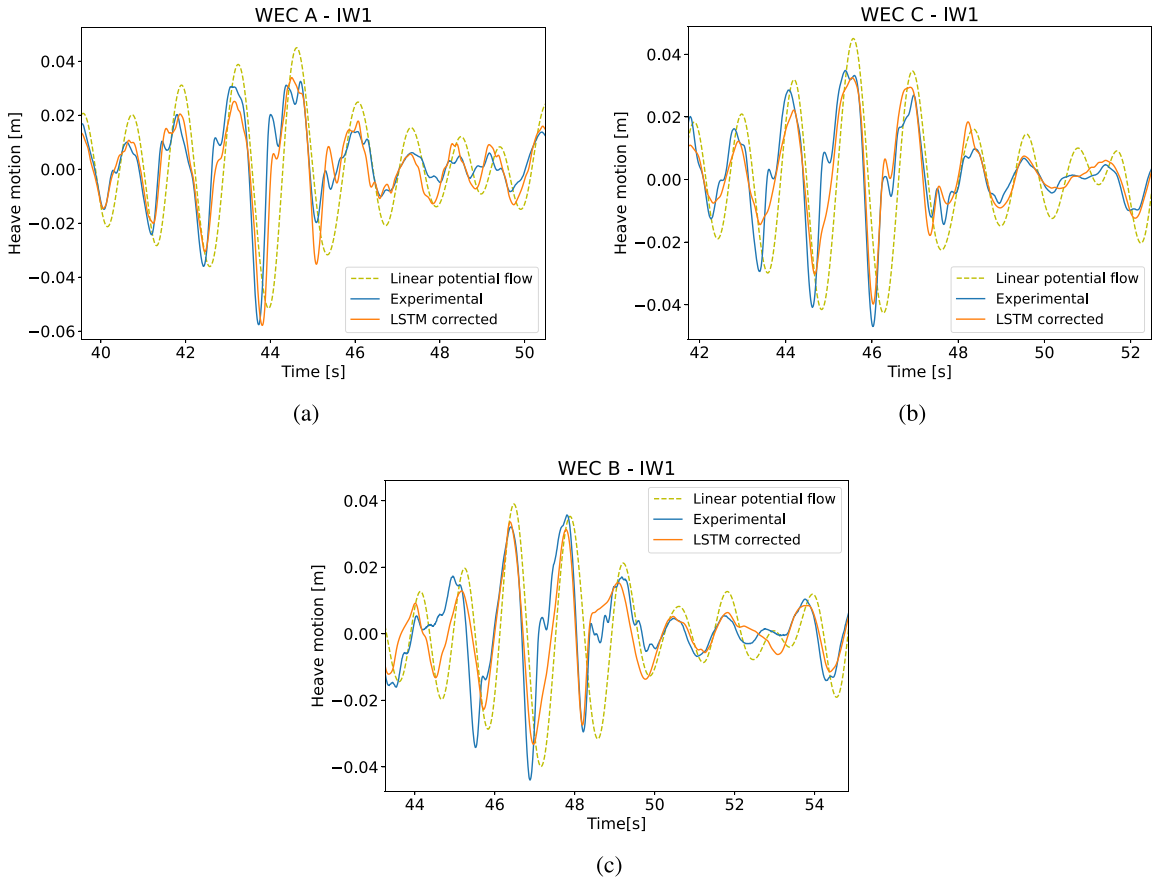

Fig. 9. In plots (a), (b), and (c), the time series of the linear potential flow, the experimental and the LSTM corrected heave motion of WECs A, C, and B, located at the bottom row of the symmetric grid in Fig. 1, are presented. The full motion of the devices is shown in response to IW1 in Table 2. We underline that in this plot, the LSTM model reconstructs the full time series of the WECs' heave motion. The motion of the WECs is plotted around the highest peak present in each sequence.

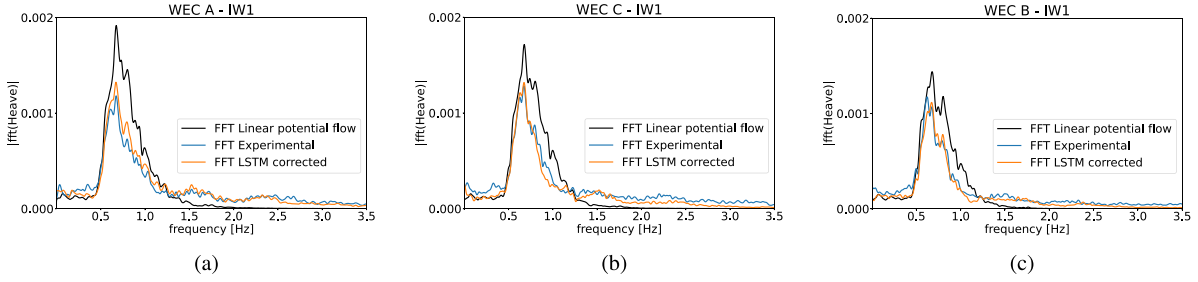

Fig. 10. Discrete Fourier transform of the linear potential flow, the LSTM corrected, and the experimental heave motion for WECs A, C, and B, located at the bottom row of the symmetric grid in Fig. 1. The spectra correspond to the heave motion presented in Fig. 9. The motion is in response to IW1, see Table 2.

for each WEC. One could notice the difference in the error norm among the interacting WECs for each irregular wave. Even though the linear potential flow scheme treats the WECs uniformly, the possible characteristic uncertainties during the experiment cannot be excluded. In Fig. 8(d), we note that the level of agreement/disagreement between the LSTM corrected and the linear potential flow model is similar across wave states IW2-IW5, while the greater correction is observed for the first sea state, namely the steepest wave IW1. Furthermore, Figs. 8(e) and 8(f) illustrate the normalized MAE for the derived velocity and acceleration of the devices in response to all the sea states tested. Note that the accuracy obtained is similar to that when analyzing the displacement estimates, validating the modeling technique for all relevant motion variables.

3.2. Validation in unseen wave conditions

All previous results in Section 3.1 are based on an LSTM model trained on the initial 70% of either time series, while the remaining 30% is used for testing. A major question arises on how the network specified in Table 3 would behave if different subsets of the available data were used for training and testing. This section aims to issue a more genuine estimate of the model's performance versus the single 70/30 percent of the train and test split specified above. To do so, we perform five separate runs, where in every assessment, the LSTM network is trained in four out of the five available irregular waves, see Table 2, while an exclusive wave is kept for testing. That is to say, the first validation run involves training the LSTM network using the whole time series corresponding to irregular waves IW2, IW3, IW4, and IW5, while the total heave motion responses corresponding to IW1 are used for testing; this validation round is indicated as V_1 (the subscript

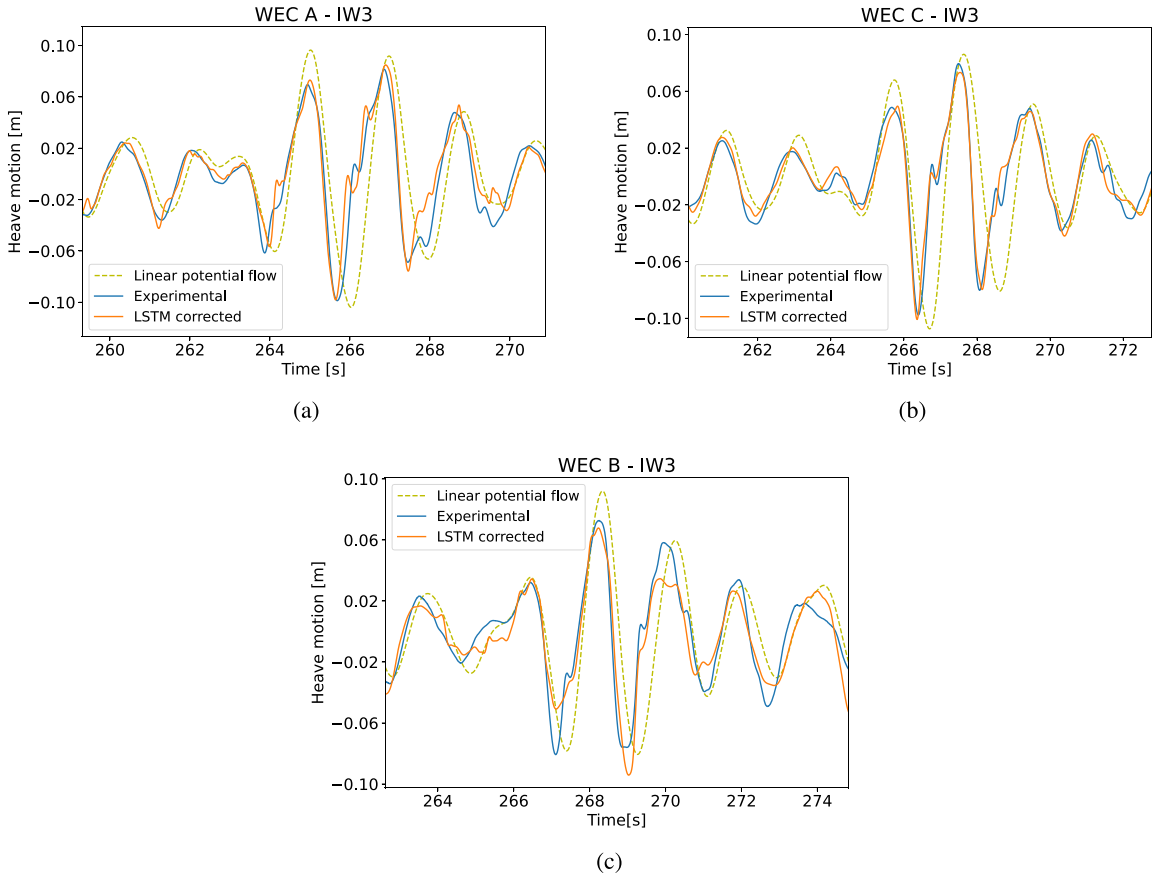

Fig. 11. In plots (a), (b), and (c), the time series of the linear potential flow, the experimental and the LSTM corrected heave motion of WECs A, C, and B, located at the bottom row of the symmetric grid in Fig. 1, are presented. The full motion of the devices is shown in response to IW3 in Table 2. We underline that in this plot, the LSTM model reconstructs the full time series of the WECs' heave motion. The motion of the WECs is plotted around the highest peak present in each sequence.

denotes the wave kept out for validation). The same process is followed for the validation runs of V_2, V_3, V_4, and V_5, see Table 4. In practice, the circulation of testing and training segments continues until each entire irregular wave in Table 2 is held out for evaluation. The design of the validation runs is not random. One of the novelties in this work lies in the ability of the LSTM network to model the nonlinear dynamics within wave energy farms in completely unseen wave environments. We underline that the extrapolation properties of the network rely heavily on the design of the training dataset. In our case, a 20% reduction in the required experimental data is achieved, so the model extrapolation is performed on a single sea state, as the wave conditions used within the experimental campaign show significant differences in the wave period. In Table 4, we compute the normalized MAE according to Eq. (6) for every interacting WEC during all the validation rounds. We underline that in this section, the LSTM model reconstructs the full time series of the WECs' heave motion in response to each tested irregular wave. Note that in Table 4, the normalized MAE is computed both for the linear potential flow heave displacement and the LSTM corrected heave displacement against the experimental motion for each WEC; in most of the cases, a correction of about 50% is achieved. We now consider the steepest sea state in more detail. The heave motion for WECs A, C, and B in response to IW1 is reconstructed using the available data from IW2, IW3, IW4, and IW5, see Figs. 9(a)–9(c). Evaluating the nonlinear behavior of the improved data is essential, so in Figs. 10(a)–10(c), the discrete Fourier transform of the linear potential flow, the LSTM corrected, and the experimental heave motion for WECs A, C, and B, in response to the steepest wave IW1 is plotted. We note that the spectra correspond to the full time series of the heave motion for all WECs. We see that the linear potential flow model cannot capture well the peaks of the spectra nor the motion of the devices in the higher frequencies. In contrast, in the LSTM corrected solution, the motion is distributed differently, capturing the peaks while catching the signal's high frequencies, namely the components that give the nonlinear behavior and the formation of the ripples, which can be seen in the high-fidelity experimental data. We further show the sea state in the middle of the wave range as the corrected time series for WECs A, C, and B in response to IW3 are obtained by training the network using the available data for IW1, IW2, IW4, and IW5, see Figs. 11(a)–11(c). In Figs. 12(a)–12(c) we plot the discrete Fourier transform of the corrected motion in response to the entire IW3.

Our model could be of great interest within the wave energy sector by providing nonlinear dynamics among multiple interacting WECs while keeping the computational efficiency of a reduced-order model. We could emphasize that the available sea states during the experiment show significant differences regarding wave steepness. Also, each sea state is represented by a single irregular wave. The reader could use our proposed method while designing an experimental dataset with similar sea states or using several waves within a single state. This way, the suggested LSTM scheme could give very strong corrections to the dynamics, as the training and evaluation wave environments would show similar stochastic characteristics. By arranging a targeted, experimental campaign employing a few closely related wave environments, together with our LSTM correction method, the user could very accurately predict the nonlinear responses of several interacting WECs in any relatable wave environment only by supplying the dynamics using any low-fidelity input.

4. Conclusions

In this study, we introduce a multi-fidelity surrogate approach to predict the nonlinear dynamic heave responses of several interacting

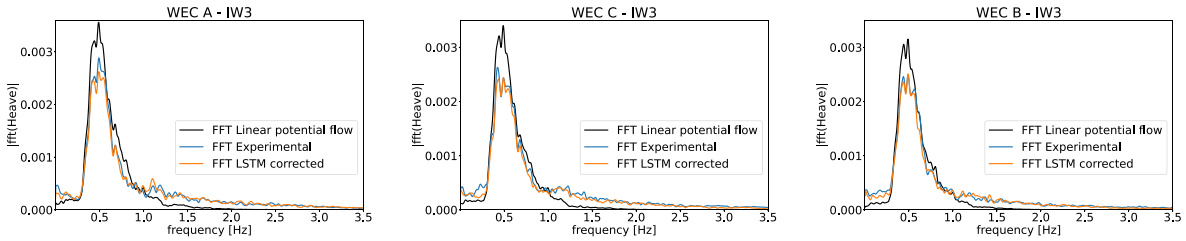

Fig. 12. Discrete Fourier transform of the linear potential flow, the LSTM corrected, and the experimental heave motion for WECs A, C, and B, located at the bottom row of the symmetric grid in Fig. 1. The spectra correspond to the heave motion presented in Fig. 9. The motion is in response to IW3, see Table 2.

Table 4
The normalized MAE (NMAE) for WECs A, C, and B in all the validation rounds for unseen wave conditions. On the left side, the NMAE of the linear potential flow (LPF) versus the experimental heave displacement is computed. On the right side, the NMAE of the LSTM corrected versus the experimental heave displacement is computed, the latter always being our ground truth. The error is normalized with the maximum value of the corresponding experimental heave motion of each WEC.

Validation	NMAE – LPF vs Experimental			NMAE – LSTM vs Experimental		
Round	WEC A	WEC C	WEC B	WEC A	WEC C	WEC B
V_1	0.125	0.140	0.140	0.062	0.075	0.072
V_2	0.092	0.090	0.092	0.045	0.052	0.049
V_3	0.085	0.089	0.099	0.040	0.050	0.056
V_4	0.083	0.102	0.085	0.041	0.059	0.051
V_5	0.095	0.113	0.096	0.053	0.072	0.069

WECs. Traditional methods to capture the complex behavior within wave energy farms usually rely on oversimplified numerical schemes incorporating linear potential flow approximations. Commonly, such numerical simulations only give a general trend as the solution deviates from reality. On the other hand, experimental data can capture the actual WEC dynamics. However, such investigations are often cost-prohibitive. In certain scenarios, even though experimental measurements are available, the accessibility is often quite limited, incorporating only a few operational conditions. Our multi-fidelity surrogate method faces two important challenges in the wave energy sector: the restricted accessibility to realistic data and the need for actual performance evaluation of wave energy generating technologies. We suggest a fusion technique by leveraging a multi-fidelity dataset that merges low-fidelity simulation results coming from a linear potential flow model and high-fidelity experimental measurements. In particular, the multi-fidelity approach incorporates an LSTM neural network that maps the low-fidelity heave responses of multiple interacting WECs to the devices' real-time, experimental heave. In a nutshell, the LSTM simulates the complex relationship between a low-fidelity input and a high-fidelity output. We highlight that the low-fidelity model is simplified in several aspects: linear potential flow theory and heave-only, while the multi-fidelity surrogate model estimates the *actual* heave motion resulting from the movement of the devices in six degrees of freedom. Following the multi-fidelity method, we can effectively simulate the nonlinear dynamic responses of multiple interacting WECs operating in diverse sea states while retaining the computational efficiency of a reduced-order model. Practically, by supplying a low-fidelity motion estimate as input, the LSTM model can predict realistic responses that closely match the experimental observations. We highlight that even though our aim in the current study is accurate motion prediction, the proposed framework can be extended to include any dynamic WEC scenario, such as power absorption or estimation of mooring line loads. To emphasize, this method can be used to acquire the *actual* wave farm performance in real-time by predicting the dynamics and capturing the actual hydrodynamic and nonlinear effects due to the intense device interaction.

CRediT authorship contribution statement

Charitini Stavropoulou: Writing – original draft, Validation, Software, Methodology, Investigation, Formal analysis, Conceptualization. **Eirini Katsidoniotaki:** Writing – review & editing, Validation, Software, Methodology, Investigation, Formal analysis, Conceptualization. **Nicolás Faedo:** Writing – review & editing, Validation, Software, Methodology, Investigation, Formal analysis, Conceptualization. **Malin Göteman:** Writing – review & editing, Supervision, Software, Project administration, Methodology, Investigation, Formal analysis.

Declaration of competing interest

The authors declare that they have no known competing financial interests or personal relationships that could have appeared to influence the work reported in this paper.

Acknowledgments

The research was supported by the Swedish Research Council (grant 2020-03634). The LSTM simulations were enabled by resources provided by the Swedish National Infrastructure for Computing (SNIC) and the National Academic Infrastructure for Supercomputing in Sweden (NAISS) at the high-performance computing cluster Tetralith at the National Supercomputer Centre at Linköping University, partially funded by the Swedish Research Council through grant agreement no. 2022-06725. Eirini Katsidoniotaki acknowledges the project funded by the Knut and Alice Wallenberg Foundation Postdoctoral Scholarship Program at MIT - KAW 2022.0334. Nicolás Faedo acknowledges the project funded by the European Union - NextGenerationEU under the National Recovery and Resilience Plan (NRRP), Mission 04 Component 2 Investment 3.1 | Project Code: IR0000027 - CUP: B33C22000710006 - iENTRANCE@ENL: Infrastructure for Energy TRAnsition aNd Circular Economy @ EuroNanoLab.

Data availability

Data will be made available on request.

References

[1] European Commission, Directorate-General for Energy, Hørman M, Georgiev I, Wessel R, Jespersen M, et al. Eu's global leadership in renewables – final synthesis report – july 2021. Publications Office of the European Union; 2022, http://dx.doi.org/10.2833/523799.

[2] Maria-Arenas A, Garrido AJ, Rusu E, Garrido I. Addendum: Maria-Arenas, A. others, control strategies applied to wave energy converters: State of the art. Energies 2019, 12, 3115. Energies 2020;13(7). http://dx.doi.org/10.3390/en13071665, URL https://www.mdpi.com/1996-1073/13/7/1665.

[3] Mork G, Barstow S, Kabuth A, Pontes MT. Assessing the global wave energy potential. In: International conference on offshore mechanics and arctic engineering, vol. 49118. 2010, p. 447–54. http://dx.doi.org/10.1115/OMAE2010-20473.

[4] Gunn K, Stock-Williams C. Quantifying the global wave power resource. Renew Energy 2012;44:296–304. http://dx.doi.org/10.1016/j.renene.2012.01.101, URL https://www.sciencedirect.com/science/article/pii/S0960148112001310.

[5] Reguero B, Losada I, Mendez F. A global wave power resource and its seasonal, interannual and long-term variability. Appl Energy 2015;148. http://dx.doi.org/10.1016/j.apenergy.2015.03.114.

[6] Gubesch E, Sergiienko NY, Nader J-R, Ding B, Cazzolato B, Penesis I, et al. Experimental investigation of a co-located wind and wave energy system in regular waves. Renew Energy 2023;219:119520. http://dx.doi.org/10.1016/j.renene.2023.119520, URL https://www.sciencedirect.com/science/article/pii/S0960148123014350.

[7] Jonasson E, Fjellstedt C, Temiz I. Grid impact of co-located offshore renewable energy sources. Renew Energy 2024;120784. http://dx.doi.org/10.1016/j.renene.2024.120784, URL https://www.sciencedirect.com/science/article/pii/S0960148124008528.

[8] Copping AE, Hemery LG, Overhus DM, Garavelli L, Freeman MC, Whiting JM, et al. Potential environmental effects of marine renewable energy development—The state of the science. J Marine Sci Eng 2020;8(11). http://dx.doi.org/10.3390/jmse8110879, URL https://www.mdpi.com/2077-1312/8/11/879.

[9] Inger R, Attrill M, Bearhop S, Broderick A, Grecian W, Hodgson D, et al. Marine renewable energy: Potential benefits to biodiversity? An urgent call for research. J Appl Ecol 2009;46:1145–53. http://dx.doi.org/10.1111/j.1365-2664.2009.01697.x.

[10] Folley M, Babarit A, Child B, Forehand D, O'Boyle L, Silverthorne K, et al. A review of numerical modelling of wave energy converter arrays. In: ASME 2012 international conference on ocean, offshore and artic engineering. Rio de Janeiro, Brazil; 2012, p. 535–45. http://dx.doi.org/10.1115/OMAE2012-83807, URL https://hal.science/hal-01202077.

[11] Leijon M, Boström C, Danielsson O, Gustafsson S, Haikonen K, Langhamer O, et al. Wave energy from the North Sea: Experiences from the Lysekil research site. Surveys Geophys 2008;29(3):221–40.

[12] Drew B, Plummer A, Sahinkaya M. A review of wave energy converter technology. Proc Instit Mech Eng A- J Power Energy 2009;223:887–902. http://dx.doi.org/10.1243/09576509JPE782.

[13] Göteman M, Giassi M, Engström J, Isberg J. Advances and challenges in wave energy park optimization—a review. Front Energy Res 2020;8:26.

[14] Crespo A, Tagliafierro B, Martínez-Estévez I, Domínguez JM, deCastro M, Gómez-Gesteira M, et al. On the state-of-the-art of CFD simulations for wave energy converters within the open-source numerical framework of DualSPHysics. In: Proceedings of the European wave and tidal energy conference, vol. 15. 2023, http://dx.doi.org/10.36688/ewtec-2023-145, URL https://submissions.evolvingcities.org/proc-ewtec/article/view/145.

[15] Katsidoniotaki E, Shahroozi Z, Eskilsson C, Palm J, Engström J, Göteman M. Validation of a CFD model for wave energy system dynamics in extreme waves. Ocean Eng 2023;268:113320.

[16] Ropero-Giralda P, Crespo AJ, Tagliafierro B, Altomare C, Domínguez JM, Gómez-Gesteira M, et al. Efficiency and survivability analysis of a point-absorber wave energy converter using DualSPHysics. Renew Energy 2020;162:1763–76. http://dx.doi.org/10.1016/j.renene.2020.10.012, URL https://www.sciencedirect.com/science/article/pii/S0960148120315780.

[17] Quartier N, Vervaet T, Fernandez GV, Domínguez JM, Crespo AJ, Stratigaki V, et al. High-fidelity numerical modelling of a two-WEC array with accurate implementation of the PTO system and control strategy using DualSPHysics. Energy 2024;296:130888. http://dx.doi.org/10.1016/j.energy.2024.130888, URL https://www.sciencedirect.com/science/article/pii/S0360544224006601.

[18] Ferziger JH, Perić M, Street RL. Computational methods for fluid dynamics. springer; 2019.

[19] Stavropoulou C, Goude A, Engström J, Göteman M. Fast time-domain model for an array of interactive point-absorbers. In: Proceedings of the European wave and tidal energy conference, vol. 15. 2023, http://dx.doi.org/10.36688/ewtec-2023-265, URL https://submissions.ewtec.org/proc-ewtec/article/view/265.

[20] Lamont-Kane P, Folley M, Whittaker T. Investigating uncertainties in physical testing of wave energy converter arrays. Proc Eur Wave Tidal Energy Conf 2013.

[21] Stratigaki V, Troch P, Stallard T, Forehand D, Folley M, Kofoed J, et al. Sea-state modification and heaving float interaction factors from physical modelling of arrays of wave energy converters. J Renew Sustain Energy 2015;7:061705. http://dx.doi.org/10.1063/1.4938030.

[22] Faedo N, Peña-Sanchez Y, Pasta E, Papini G, Mosquera FD, Ferri F. SWELL: An open-access experimental dataset for arrays of wave energy conversion systems. Renew Energy 2023;212:699–716. http://dx.doi.org/10.1016/j.renene.2023.05.069, URL https://www.sciencedirect.com/science/article/pii/S0960148123006924.

[23] Giassi M, Göteman M. Layout design of wave energy parks by a genetic algorithm. Ocean Eng 2018;154:252–61. http://dx.doi.org/10.1016/j.oceaneng.2018.01.096.

[24] Babarit A. On the park effect in arrays of oscillating wave energy converters. Renew Energy 2013;58:68–78. http://dx.doi.org/10.1016/j.renene.2013.03.008, URL https://www.sciencedirect.com/science/article/pii/S096014811300164X.

[25] Giassi M, Castellucci V, Göteman M. Economical layout optimization of wave energy parks clustered in electrical subsystems. Appl Ocean Res 2020;101:102274. http://dx.doi.org/10.1016/j.apor.2020.102274.

[26] Castro-Santos L, Filgueira-Vizoso A, Costoya X, Arguilé-Pérez B, Ribeiro AS. Economic viability of floating wave power farms considering the energy generated in the near future. Renew Energy 2024;222:119947. http://dx.doi.org/10.1016/j.renene.2024.119947, URL https://www.sciencedirect.com/science/article/pii/S0960148124000120.

[27] Atan R, Finnegan W, Nash S, Goggins J. The effect of arrays of wave energy converters on the nearshore wave climate. Ocean Eng 2019;172:373–84. http://dx.doi.org/10.1016/j.oceaneng.2018.11.043, URL https://www.sciencedirect.com/science/article/pii/S0029801818321140.

[28] Devolder B, Rauwoens P, Troch P. Towards the numerical simulation of 5 floating point absorber wave energy converters installed in a line array using openfoam. In: Proceedings of the 12th wave and tidal energy conference. 2017, p. 739–49.

[29] Shahroozi Z, Göteman M, Engström J. Control of a point absorber wave energy converter in extreme wave conditions using a deep learning model in WEC-sim. In: OCEANS 2023 - limerick. 2023, p. 1–10. http://dx.doi.org/10.1109/OCEANSLimerick52467.2023.10244529.

[30] Pasta E, Papini G, Peña-Sanchez Y, Mosquera FD, Ferri F, Faedo N. Data-based modelling of arrays of wave energy systems: Experimental tests, models, and validation. Control Eng Pract 2024;148:105949. http://dx.doi.org/10.1016/j.conengprac.2024.105949, URL https://www.sciencedirect.com/science/article/pii/S0967066124001096.

[31] Ringwood JV, Bacelli G, Fusco F. Energy-maximizing control of wave-energy converters: The development of control system technology to optimize their operation. IEEE Control Syst Mag 2014;34(5):30–55. http://dx.doi.org/10.1109/MCS.2014.2333253.

[32] Ringwood JV, Zhan S, Faedo N. Empowering wave energy with control technology: Possibilities and pitfalls. Annu Rev Control 2023;55:18–44. http://dx.doi.org/10.1016/j.arcontrol.2023.04.004, URL https://www.sciencedirect.com/science/article/pii/S1367578823000226.

[33] Said HA, Ringwood JV. Grid integration aspects of wave energy—Overview and perspectives. IET Renew Power Gener 2021;15(14):3045–64. http://dx.doi.org/10.1049/rpg2.12179, URL https://ietresearch.onlinelibrary.wiley.com/doi/abs/10.1049/rpg2.12179.

[34] Penalba M, Ringwood JV. A high-fidelity wave-to-wire model for wave energy converters. Renew Energy 2019;134:367–78. http://dx.doi.org/10.1016/j.renene.2018.11.040, URL https://www.sciencedirect.com/science/article/pii/S0960148118313600.

[35] Wang L, Isberg J, Tedeschi E. Review of control strategies for wave energy conversion systems and their validation: the wave-to-wire approach. Renew Sustain Energy Rev 2018;81:366–79. http://dx.doi.org/10.1016/j.rser.2017.06.074, URL https://www.sciencedirect.com/science/article/pii/S136403211731016X.

[36] Wang Z, Qiao D, Yan J, Tang G, Li B, Ning D. A new approach to predict dynamic mooring tension using LSTM neural network based on responses of floating structure. Ocean Eng 2022;249:110905. http://dx.doi.org/10.1016/j.oceaneng.2022.110905, URL https://www.sciencedirect.com/science/article/pii/S0029801822003419.

[37] Qiao D, Li P, Ma G, Qi X, Yan J, Ning D, et al. Realtime prediction of dynamic mooring lines responses with LSTM neural network model. Ocean Eng 2021;219:108368. http://dx.doi.org/10.1016/j.oceaneng.2020.108368, URL https://www.sciencedirect.com/science/article/pii/S0029801820312750.

[38] Saad AM, Schopp F, Barreira RA, Santos IHF, Tannuri EA, Gomi ES, et al. Using neural network approaches to detect mooring line failure. IEEE Access 2021;9:27678–95. http://dx.doi.org/10.1109/ACCESS.2021.3058592.

[39] Katsidoniotaki E, Guth S, Göteman M, Sapsis TP. Reduced order modeling of wave energy systems via sequential Bayesian experimental design and machine learning. 2023.

[40] Mousavi SM, Ghasemi M, Dehghan Manshadi M, Mosavi A. Deep learning for wave energy converter modeling using long short-term memory. Mathematics 2021;9(8). http://dx.doi.org/10.3390/math9080871, URL https://www.mdpi.com/2227-7390/9/8/871.

[41] Ahmed AAM, Jui SJ, AL-Musaylh MS, Raj N, Saha R, Deo RC, Saha SK. Hybrid deep learning model for wave height prediction in Australia's wave energy region. Appl Soft Comput 2024;150:111003. http://dx.doi.org/10.1016/j.asoc.2023.111003, URL https://www.sciencedirect.com/science/article/pii/S1568494623010219.

[42] Silva KM, Maki KJ. Data-driven system identification of 6-DoF ship motion in waves with neural networks. Appl Ocean Res 2022;125:103222. http://dx.doi.org/10.1016/j.apor.2022.103222, URL https://www.sciencedirect.com/science/article/pii/S0141118722001614.

[43] Xu W, Maki KJ, Silva KM. A data-driven model for nonlinear marine dynamics. Ocean Eng 2021;236:109469. http://dx.doi.org/10.1016/j.oceaneng.2021.109469, URL https://www.sciencedirect.com/science/article/pii/S0029801821008726.

[44] del Águila Ferrandis J, Triantafyllou M, Chryssostomidis C, Karniadakis G. Learning functionals via LSTM neural networks for predicting vessel dynamics in extreme sea states. Proc Royal Soc A: Math Phys Eng Sci 2021;477:20190897. http://dx.doi.org/10.1098/rspa.2019.0897.

[45] Conti P, Guo M, Manzoni A, Hesthaven JS. Multi-fidelity surrogate modeling using long short-term memory networks. Comput Methods Appl Mech Engrg 2023;404:115811.

[46] Conti P, Guo M, Manzoni A, Frangi A, Brunton SL, Kutz JN. Multi-fidelity reduced-order surrogate modeling. 2023, arXiv:2309.00325.

[47] Perdikaris P, Raissi M, Damianou A, Lawrence N, Karniadakis G. Nonlinear information fusion algorithms for data-efficient multi-fidelity modelling. Proc Royal Soc A: Math Phys Eng Sci 2017;473:20160751. http://dx.doi.org/10.1098/rspa.2016.0751.

[48] Kennedy M, O'Hagan A. Predicting the output from a complex computer code when fast approximations are available. Biometrika 1998;87. http://dx.doi.org/10.1093/biomet/87.1.1.

[49] Le Gratiet L, Garnier J. Recursive co-kriging model for design of computer experiments with multiple levels of fidelity. Int J Uncertain Quant 2014;4(5):365–86, URL https://hal.science/hal-01108813.

[50] Meng X, Karniadakis GE. A composite neural network that learns from multi-fidelity data: Application to function approximation and inverse PDE problems. J Comput Phys 2020;401:109020. http://dx.doi.org/10.1016/j.jcp.2019.109020, URL https://www.sciencedirect.com/science/article/pii/S0021999119307260.

[51] Giannoukou K, Marelli S, Sudret B. A comprehensive framework for multi-fidelity surrogate modeling with noisy data: a gray-box perspective. 2024, arXiv:2401.06447.

[52] Meng X, Babaee H, Karniadakis GE. Multi-fidelity Bayesian neural networks: Algorithms and applications. J Comput Phys 2021;438:110361. http://dx.doi.org/10.1016/j.jcp.2021.110361, URL https://www.sciencedirect.com/science/article/pii/S0021999121002564.

[53] Katsidoniotaki E, Su B, Kelasidi E, Sapsis TP. Multifidelity digital twin for real-time monitoring of structural dynamics in aquaculture net cages. 2024, arXiv:2406.04519.

[54] Levine MD, Edwards SJ, Howard D, Weems K, Sapsis TP, Pipiras V. Multi-fidelity data-adaptive autonomous seakeeping. Ocean Eng 2024;292:116322. http://dx.doi.org/10.1016/j.oceaneng.2023.116322, URL https://www.sciencedirect.com/science/article/pii/S0029801823027063.

[55] Huang S, Liu W-q, Wang K, Wu T-c, Liu T-h. Shape optimization design of a heaving buoy of wave energy converter based on fully parametric modeling and CFD method. J Hydrodyn 2022;34. http://dx.doi.org/10.1007/s42241-022-0080-x.

[56] Penalba M, Merigaud A, Gilloteaux J-c, Ringwood J. Nonlinear froude-krylov force modelling for two heaving wave energy point absorbers. 2015.

[57] Beringer C, Bosma B, Robertson B. Degrees of freedom effects on a laboratory scale WEC point absorber. In: Proceedings of the European wave and tidal energy conference, vol. 15. 2023, http://dx.doi.org/10.36688/ewtec-2023-380.

[58] Giassi M, Engström J, Isberg J, Göteman M. Comparison of wave energy park layouts by experimental and numerical methods. J Marine Sci Eng 2020;8(10). http://dx.doi.org/10.3390/jmse8100750, URL https://www.mdpi.com/2077-1312/8/10/750.

[59] Thomas S, Giassi M, Göteman M, Hann M, Ransley E, Isberg J, et al. Performance of a direct-driven wave energy point absorber with high inertia rotatory power take-off. Energies 2018;11:2332. http://dx.doi.org/10.3390/en11092332.

[60] Cummins W. The impulse response function and ship motions, vol. 9, 1962, p. 101–9.

[61] Wazwaz A-M. Volterra integro-differential equations. In: Linear and nonlinear integral equations: methods and applications. Springer; 2011, p. 175–212.

[62] Stavropoulou C, Engström J, Göteman M. Two-body, time domain model for a heaving point absorber. In: Advances in the analysis and design of marine structures: proceedings of the 9th international conference on marine structures (MARSTRUCT), Gothenburg, Sweden.. 2023.

[63] Stavropoulou C, Goude A, Katsidoniotaki E, Göteman M. Fast time-domain model for the preliminary design of a wave power farm. Renew Energy 2023;219:119482. http://dx.doi.org/10.1016/j.renene.2023.119482, URL https://www.sciencedirect.com/science/article/pii/S0960148123013976.

[64] Pasta E, Papini G, Peña-Sanchez Y, Mosquera FD, Ferri F, Faedo N. Data-based modelling of arrays of wave energy systems: Experimental tests, models, and validation. Control Eng Pract 2024;148:105949.

[65] Pintelon R, Schoukens J. System identification: a frequency domain approach. John Wiley & Sons; 2012.

[66] Hochreiter S, Schmidhuber J. Long short-term memory. Neural Comput 1997;9:1735–80, URL https://api.semanticscholar.org/CorpusID:1915014.

[67] Kingma DP, Ba J. Adam: A method for stochastic optimization. 2014, arXiv preprint arXiv:1412.6980.